PERGAMON

International Journal of Solids and Structures 40 (2003) 2147–2170

INTERNATIONAL JOURNAL OF SOLIDS and STRUCTURES

www.elsevier.com/locate/ijsolstr

Dynamic response and energy dissipation characteristics of balsa wood: experiment and analysis

M. Vural [a,b,*], G. Ravichandran [a]

[a] *Graduate Aeronautical Laboratories, California Institute of Technology, 1200 E. California Blvd., Pasadena, CA 91125, USA*
[b] *Department of Aeronautical Engineering, Istanbul Technical University, Maslak, Istanbul 80626, Turkey*

Received 19 April 2002; received in revised form 7 January 2003

Abstract

Dynamic response of a cellular sandwich core material, balsa wood, is investigated over its entire density spectrum ranging from 55 to 380 kg/m^3. Specimens were compression loaded along the grain direction at a nominal strain rate of 3×10^3 s^{-1} using a modified Kolsky (split Hopkinson) bar. The dynamic data are discussed and compared to those of quasi-static experiments reported in a previous study (Mech. Mater. 35 (2003) 523). Results show that while the initial failure stress is very sensitive to the rate of loading, plateau (crushing) stress remains unaffected by the strain rate. As in quasi-static loading, buckling and kink band formation were identified to be two major failure modes in dynamic loading as well. However, the degree of dynamic strength enhancement was observed to be different for these two distinct modes. Kinematics of deformation of the observed failure modes and associated micro-inertial effects are modeled to explain this different behavior. Specific energy dissipation capacity of balsa wood was computed and is found to be comparable with those of fiber-reinforced polymer composites.

Keywords: Balsa wood; Cellular materials; Impact energy dissipation; High-strain-rate; Micro-inertia; Failure model

1. Introduction

Cellular materials with stochastic (closed or open cell foams) and periodic (regular micro-truss architectures or 2D periodic channels such as honeycombs) topologies are often utilized as sandwich core materials in shock attenuation and impact damage protection applications (Gibson and Ashby, 1997; Ashby et al., 2000). In these applications, energy is transmitted to the system mostly by the impact of a foreign object and dissipated through the compressive inelastic deformation of cells within the material. Flow (crushing) stress of the cellular material determines the load transmitted to the system during dissipation process and the deceleration of the impactor as well. Thus, it is desired to be kept at an optimum level, which is not too high to damage the structure and its contents and not too low to diminish the amount of energy dissipated. Once the flow stress is established, the ultimate deformation (or the maximum strain

* Corresponding author. Tel.: +1-626-395-4748; fax: +1-626-449-6359.
E-mail address: mvural@its.caltech.edu (M. Vural).

0020-7683/03/$ - see front matter © 2003 Elsevier Science Ltd. All rights reserved.
doi:10.1016/S0020-7683(03)00057-X

before stress elevation) determines the amount of energy that can be dissipated safely. Therefore, the constitutive response of an ideal energy dissipator is that of a rigid–perfectly plastic material capable of tolerating very large strains. Within this framework, balsa wood, as a naturally occurring porous bio-composite, offers salient mechanical and physical properties. As its cellular/porous microstructure allows the application of large deformations, fine composite nano-architecture of wood cell material increases its specific strength and stiffness, giving rise to a high specific energy dissipation capacity. Moreover the fact that balsa wood can be found in a wide range of densities from 40 to 380 kg/m^3, depending on the average size and the wall thickness of cells, provides the flexibility in design since the strength is a monotonic function of its density (Vural and Ravichandran, 2003).

Several uniaxial quasi-static experimental investigations have been carried out to determine the mechanical properties and deformation mechanisms of balsa wood in longitudinal and/or transverse directions by Knoell (1966), Soden and McLeish (1976), Easterling et al. (1982) and Vural and Ravichandran (2003). Knoell (1966) investigated the effects of environmental and physical variables (temperature, moisture content and ambient pressure) on the mechanical response of balsa wood. Soden and McLeish (1976) carried out an extensive investigation, which mainly concentrated on the variation of tensile strength with fiber alignment. They also reported compressive strength data. Easterling et al. (1982) paid particular attention to the micromechanics of deformation in their experiments, during which they performed in situ scanning electron microscopy (SEM) observations and defined the end-cap collapse of grains as the dominant compressive failure mechanism in longitudinal direction. Vural and Ravichandran (2003) documented the compressive strength, plateau stress and densification strain of balsa wood in its entire density range, identified the variations in failure mechanisms with density and described simple analytical models to represent the observed experimental strength data. However, the dynamic compression behavior of balsa wood (and in general wood) has received limited attention. Daigle and Lonborg (1961) performed dynamic compression experiments on balsa wood and several other crushable materials using drop towers and compared their specific energy absorption capacities. Recently, Reid and Peng (1997) investigated the dynamic crushing behavior of several wood species, including balsa wood, through the impact of free flying specimens on a rigid wall. While their tests covered a wide range of impact velocities up to approximately 300 m/s, they tested the specimens at a certain density for each species. Therefore, a systematic investigation on the dynamic response of balsa wood for different strain rates and specimen densities that covers its entire range is still lacking.

In this paper, the dynamic response of balsa wood is investigated at a nominal strain rate of 3×10^3 s^{-1} over its entire density range and the results are discussed in conjunction with the quasi-static data reported in a previous study (Vural and Ravichandran, 2003). In Section 2, microstructural features of balsa wood, specimen preparation and the experimental method for dynamic loading are described. Experimental results and the detailed discussion of mechanical response and micromechanics of deformation are given in Section 3. In this section, particular emphasis has been given to the understanding of the source of dynamic strength enhancement, the energy dissipation characteristics and their dependence on the density and dominant failure modes. In Section 4, based on the kinematics of deformation modes at cellular scale, models are developed to quantify the contribution of micro-inertia to dynamic strength enhancement. In Section 5, model predictions and experimental results are compared and shown to have good correlation.

2. Materials and methods

2.1. Microstructural features of balsa wood

As shown in Fig. 1, the cellular microstructure of balsa (*Ochroma*) is mainly composed of long prismatic cells (fibers, grains) of nearly honeycomb shape and the blocks of these cells are separated by narrower rays

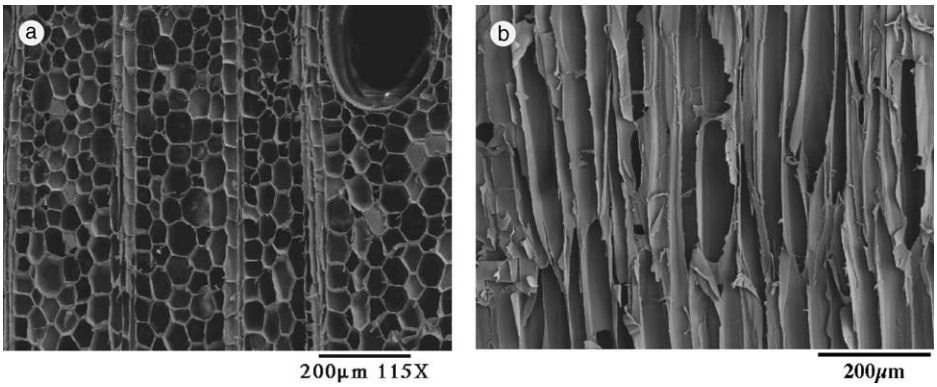

Fig. 1. Scanning electron micrographs showing typical (a) across the grain and (b) along the grain cross-sections of balsa wood.

in which the cells are smaller and of a different shape. Balsa wood has three orthogonal axes in the longitudinal (L, along the grain), radial (R, across the grain and along the rays) and tangential (T, across the grain and transverse to rays) directions forming a heterogeneous porous composite. This composite is highly anisotropic with a high ratio of longitudinal to transverse properties, the latter having also difference in itself due to so-called ray cells oriented in radial direction. It should be noted that, for applications where balsa wood is considered as a potential material to dissipate energy, its dynamic constitutive response in longitudinal direction as well as corresponding failure mechanisms are of particular interest.

Balsa, as a diffuse-porous hardwood, has a uniform distribution in type and size of cells throughout the grain cross-section (see Fig. 1(a)). Cells of nearly hexagonal shape (grains) have diameters ranging from 30 to 70 μm, with an average of 45 μm. These long, hexagonal-prismatic cells are pointed at the ends (Fig. 1(b)) and have an average length of 650 μm, giving the cell an aspect ratio of about 16:1, as also reported by Easterling et al. (1982). Blocks of these large cells are separated by narrower rays in which the cells are smaller and of a different shape. Large sap channels running parallel to the axis of the tree penetrate the entire structure. Average diameter of sap channels is around 350 μm.

It must be noted that even though the grains in balsa wood are highly oriented in longitudinal direction this alignment is far from being perfect, as would be expected in a naturally occurring material. As also discussed by Vural and Ravichandran (2003), the major fiber misalignment is observed in LT plane of balsa wood mainly due to the existence of ray cells penetrating the complete structure in radial direction. The SEM examinations performed on the LT planes of balsa specimens with various densities shows that the maximum fiber misalignment angles are highly scattered in the range between 7° and 11°. Apart from this measurable imperfection at a length scale of the cell height, individual cell walls possess further imperfections at smaller length scales that are difficult to quantify such as the waviness or non-uniform thickness distribution along the cell walls.

2.2. Specimens

Experiments were performed on balsa wood specimens over a wide range of densities between 55 and 380 kg/m^3. Cylindrical specimens were machined from large blocks of balsa wood at five different nominal densities provided by BALTEK Corporation (Northvale, NJ) and the lateral surface was polished using 320 grit sand papers. In order to avoid any possible end effects on the mechanical behavior during testing, planar surfaces of specimens were machined and inspected with extreme care to assure good specimen end-surface quality. The specimen dimensions were typically 9.5 ± 0.12 mm in diameter and 5.08 ± 0.12 mm in length, corresponding to a length to diameter ratio of 0.53. The density of specimens was measured in a

consistent way, paying considerable attention particularly to the moisture content since it has significant effect on both density and properties (Dinwoodie, 1975). Due to the inherent variation of density within each block of a certain nominal density, specimens were prepared with densities varying continuously between the ranges specified above. In order to find moisture contents of balsa specimens a series of specimens were heat-treated in furnace at 110 °C and intermittent weight measurements were performed until they reached a constant weight. Measured moisture content ranged from 8% to 11%, which is the typical value for well-seasoned dry woods.

2.3. Experimental method

The specimens were dynamically loaded using a modified Kolsky (split Hopkinson) pressure bar as shown in Fig. 2. Kolsky pressure bar, originally developed by Kolsky (1949), has been widely used and modified to measure the dynamic compressive behavior of engineering materials. The present modification through the use of a quartz single crystal, introduced by Chen et al. (2000), enables the stress measurements three orders of magnitude more sensitive than achievable in a conventional Kolsky (split Hopkinson) pressure bar. Hence, stress profiles of low amplitudes experienced by balsa specimens could be measured with high precision by adopting this modification.

The lengths of the bars in Kolsky pressure bar setup used in this study are 1219 mm for the incident bar, and, 584 and 610 mm for the two sections of the transmission bars, with a common diameter of 12.7 mm. The striker bars of 12.7 mm diameter were used with varying lengths to achieve desired pulse duration. All the bars are made of precision ground 7075-T651 aluminum alloy. Depending on the striker velocity, either a thin, annealed copper (C11000) disc of 4.8 mm in diameter and 0.81 mm in thickness or a layer of tissue paper was typically used as pulse shaper to control the rise time of the incident pulse and to ensure stress equilibration within the specimen (Ravichandran and Subhash, 1994). A high resistance (1000 Ω) strain gage (Micromeasurements, WK-06-250BF-10C) with excitation voltage of 30 V was used to measure the surface strain on the incident bar. The raw strain gage signal was recorded using a high-speed 12-bit digital oscilloscope (Nicolet 440). A Valpey–Fisher X-cut quartz single crystal of 12.7 ± 0.025 mm in diameter and 0.254 ± 0.025 mm in thickness, coated with a 30 nm thick chrome/gold layer on both of the flat surfaces, was glued to the end of the transmission bar in contact with the specimen using a conductive epoxy (CW2400, Chemtronics). Other surface remained in contact with the other half of the transmission bar without bonding, allowing the compressive transmitted pulse to pass through the quartz disk without reflection. Before each experiment, a thin layer of conductive grease (CW7100, Chemtronics) was applied at the contact surface to ensure electrical conductivity. Thin, silver coated copper wires were wrapped and glued (using the same conductive epoxy) to the bar surface near the quartz crystal. The wires were connected to a charge amplifier (Kistler 5010B1) whose output is recorded using the digital oscilloscope for data processing.

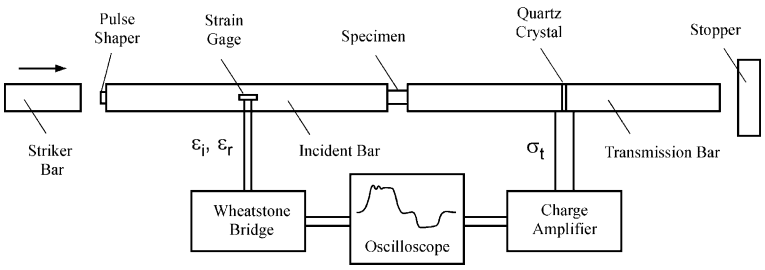

Fig. 2. Schematic of a modified Kolsky (split Hopkinson) pressure bar used in the dynamic compression of balsa specimens.

Using the modified Kolsky pressure bar system described above, balsa wood specimens were uniaxially compressed in longitudinal (L) direction (i.e., along the grain) at a nominal strain rate of 3×10^3 s^{-1}.

3. Experimental results

3.1. Stress–strain response

Fig. 3 shows the representative dynamic engineering stress–strain curves of the balsa wood for several different densities. As in quasi-static response (Vural and Ravichandran, 2003), dynamic response as well is almost linear up to a maximum stress (failure strength) beyond which, as the deformation is increased, the stress level either remains nearly constant or experience a sudden drop depending mainly on the density of specimen. After this sudden drop, if there is, the specimen continues to deform at a lower level of stress (plateau stress). Eventually, at large strains, the wood cells collapse sufficiently so that opposing cell walls contact each other (or their broken fragments pack together) and further deformation compresses the cell wall material itself. This gives the final, steeply rising portion of the stress–strain curve called densification (or consolidation, locking) regime.

It should be emphasized that the quality of the loading surfaces of specimens becomes an important issue in compressive testing of cellular solids due to the so-called end effects, which may alter certain features of the mechanical behavior. Due to both frictional effects and the discrete nature of cellular topology, specimens have a tendency to premature localized deformation at the loading surfaces when the surface preparation is of poor quality. For instance, experiments on specimens with roughly cut end-surfaces may result in a lower compressive modulus when using end plate displacements than when using an extensometer because of the end effects (Ashby et al., 2000). It should be stated at this point that neither the elastic modulus nor its variation with density or strain rate has been the subject of this study. End effects are also important in that they may affect the magnitude of compressive failure strength. If the cellular solid under consideration is a type II structure (i.e., has a significant strain softening at the end of

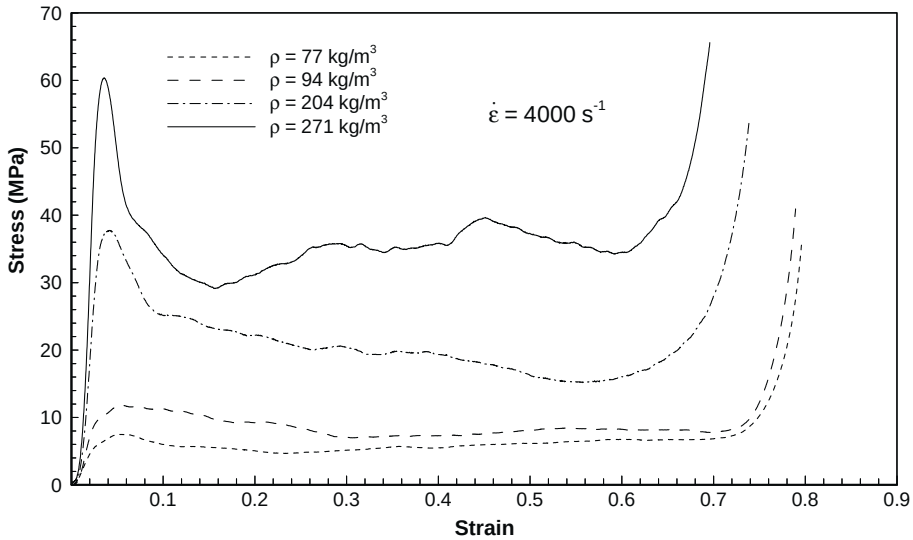

Fig. 3. Variation of dynamic response (nominal stress–strain) with the density of balsa wood.

homogeneous elastic deformation and with the beginning of initial failure localization) such as the honeycombs loaded in longitudinal direction, the geometric imperfections at the specimen ends may obscure the initial stress peak and result in monotonous stress–strain curves. In the present study, planar surfaces of cylindrical specimens have been machined and inspected with extreme care to assure good specimen-end quality and to avoid any possible end effects on the mechanical behavior during testing. Experimental stress–strain curves further verify that the end effects of this type have been avoided (Fig. 3). Finally, as long as the large strain inelastic behavior of cellular solids is concerned (such as the plateau stress and densification strain) end effects are negligible for all practical purposes. Large-strain deformation of balsa wood involves the regions of intense localization which eventually act as favored sites for progressive deformation, replacing any possible degenerative role of end effects.

3.1.1. Failure strength and plateau stress

The initial linear response of balsa wood represents the uniform elastic deformation throughout the structure. At the end of this phase, initiation of buckling or kink band formation in the weakest bands of cells defines the initial failure stress (failure strength), which corresponds to the initial peak in stress–strain curves shown in Fig. 3. At the beginning, deformation is restricted to these zones which collapse unstably until the affected cells are sufficiently and severely crushed to cause local stiffening. As will be discussed in detail below, the initial collapse of these cells reduces the strength of adjacent cells and consequently those start buckling or kink banding at a stress level slightly (or significantly for high-density specimens) smaller than the initial collapse stress. The repetition of this process results in gross deformation propagating from these initial zones of failure to the rest of cellular structure under the plateau stress. As can be seen from Fig. 3, this progressive phase of deformation does not occur ideally at a constant stress level. Therefore, plateau stress is defined in this study as the average stress that would result in the same energy dissipation between the elastic region and the densification strain for a given increment of strain.

Fig. 4 comparatively illustrates both quasi-static and dynamic data for the failure strength and the plateau stress of balsa wood. Quasi-static data were taken from Vural and Ravichandran (2003) in which the following simple models are suggested for the prediction of compressive failure strength data in longitudinal (L) direction,

$$\sigma_{\mathrm{pb}} = 2\sigma_{\mathrm{ys}}(\rho/\rho_{\mathrm{s}})^{5/3} \quad \text{for plastic buckling,} \tag{1a}$$

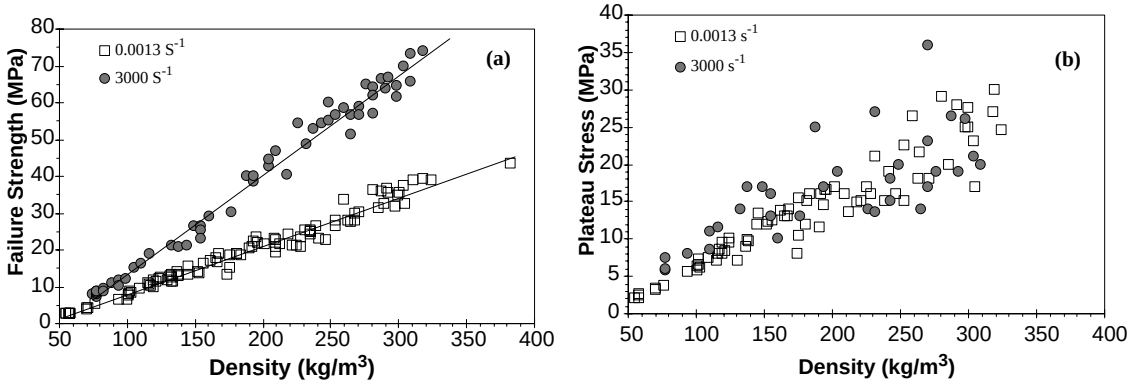

Fig. 4. Variation of (a) compressive failure strength and (b) plateau stress in balsa wood with density and strain rate.

$$\sigma_{pc} = \frac{0.5G_s(\rho/\rho_s)}{1+\frac{\theta_0}{\gamma_y}} \quad \text{for kink band formation,} \tag{1b}$$

where σ_{ys} is the yield stress of wood cell substance, ρ is the density of balsa wood, ρ_s and G_s are the density and shear modulus of wood cell substance, respectively, θ_0 is initial fiber misalignment angle, and γ_y is the yield strain of balsa wood in longitudinal shear. The typical values of $\sigma_{ys} = 350$ MPa, $\rho_s = 1500$ kg/m^3, $G_s = 2.6$ GPa, $\theta_0 = 9°$, $\gamma_y = 0.023$, are given for the variables in Eqs. (1a) and (1b) (Vural and Ravichandran, 2003). These expressions are based on experimentally observed physical mechanisms of deformation and shown to provide good predictions of the critical quasi-static stress for the initiation of failure in corresponding modes. Basically, the above expressions suggest that for a certain relative density deformation occurs in the mode that requires the lowest critical stress, which is shown to be the case through post-mortem SEM examinations of failure surfaces. It should be added that the predictions of pyramidal end-cap collapse and kink band formation models are very close to each other and there is experimental evidence suggesting that these two are interactive mechanisms rather than independent. Therefore, for quasi-static loading, two major modes of deformation are the buckling and kink band formation for low-density balsa and high-density balsa, respectively, with a transition region between 170 and 200 kg/m^3 validated by both model predictions and experimental evidence (Vural and Ravichandran, 2003).

Solid lines in Fig. 4(a) represent the best linear fits to the experimental data. It is obvious that both the density and the strain rate have considerable effects on the initial failure strength of balsa wood. Higher density means increased ratio of cell wall thickness to cell diameter, and thus less porosity, therefore its effect towards fortifying the structure is expected and experimentally observed in both failure strength and plateau stress. However, the effect of strain rate seems to be more complicated due to the fact that the plateau stress is practically insensitive to the strain rate whereas the failure strength is significantly affected by the increase in strain rate. In other words, experimental evidence indicates that, while the critical stress for failure initiation has a strong dependence on the strain rate, driving force for progressive deformation remains unaffected by the dynamics of deformation. This difference in response to increasing strain rate can simply be explained in terms of the differences in the kinematics of deformation, associated micro-inertia and initiation mechanism at micro-scale prior to initial failure and during progressive deformation. Initial failure at the peak stress level is preceded by elastic loading. Micromechanics of deformation in this regime is characterized by the uniform axial compression of wood cells in longitudinal direction. Initial failure is mostly triggered by an elastic instability in the form of local micro-buckling or kink band formation depending mainly on the density of balsa wood. In dynamic loading, the onset of both these kinds of instabilities are intimately related to the lateral inertia in deforming elements, which in turn enhances the critical stress for failure initiation in the longitudinal direction. Calculations based on the kinematics of micro-buckling/bending geometries show that even though the initial effect of this inertial-strain-rate hardening is very strong it rapidly falls off and becomes negligible during the evolution of deformation in a localized zone. However, progressive deformation phase is also characterized, in addition to the continuation of deformation in initially localized regions, by the creation of new localization zones. Following the initial failure/localization, the state of stress experienced by neighboring cells is perturbed and far from being uniaxial due to the kinematics of deformation at the micro-scale. This new local situation (state of stress) makes the subsequent progressive deformation (localizations) easier and at a lower nominal stress level by taking and exaggerating, in a sense, the role of local geometric and material imperfections that trigger the initial failure. Within this framework, regarding the formation of new strain localization sites, it appears that the softening effect due to the perturbations in stress field created by preceding localization suppresses the effect of inertial hardening. The effect of strain rate, and hence micro-inertia, is thus restricted to the initiation phase of first instability due to the kinematics of failure (buckling/kink banding). During the following progressive deformation phase the effect of inertia is suppressed either by the

kinematical considerations, as in the evolution of deformation within localized region, or by the perturbations in stress field as in the creation of new localization sites.

Fig. 4(b) also shows an increased scatter in plateau stress when the specimen density exceeds 170–200 kg/m^3 interval. This is attributed to the transition in deformation mode from micro-buckling to kink band formation and resulting increased susceptibility of plateau stress to the random nature of increased perturbations in stress field. As the length scale of the deformation geometry increases from a fraction of cell diameter in buckling mode to as much as 10–15 times the cell diameter in kink band formation mode, an increased level of perturbation is induced in the stress field and it generates the increased scatter in plateau stress for denser specimens.

3.1.2. Densification (consolidation, locking) strain

At the end of plateau region after all cells have collapsed, densification strain is reached and continued compression results in the compaction of deformed and ruptured cell walls against each other, leading to rapid increase in crushing stress since internal voids are almost eliminated. For design purpose, densification strain can be interpreted as the maximum range of safe loading in the sense that beyond this range further compression generates substantial amplification in the stress level over the plateau stress as well as initial failure strength. Therefore, in applications where shock attenuation and impact damage protection are considered to be of significant importance, densification strain is one of the important material properties because, together with plateau stress, they directly determine the energy absorption capacity of material.

Fig. 5 illustrates the effects of initial density and strain rate on the densification strain of balsa wood, which is defined in this study as the strain at the last local minimum before the stress starts rising steeply (see also Fig. 3). For quasi-static loading rates, densification strain decreases as a function of specimen density and varies between 0.68 and 0.86. As expected, the denser is the balsa wood the lower is the densification strain due to its close correlation with the level of initial porosity. In dynamic loading regime, the same declining linear trend in densification strain is preserved. However, it is shifted downwards and the

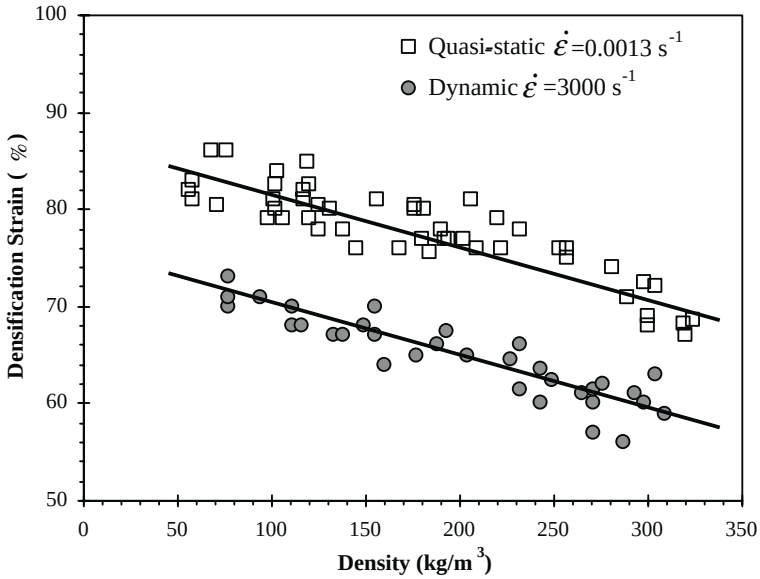

Fig. 5. Decreasing trend of densification strain in balsa wood with density and strain rate.

bounds decrease to the range between 0.58 and 0.74, suggesting that cellular packing efficiency at the microstructural level degrades by the increasing rate of strain. This could be attributed to the micro-inertial effect associated with the cell wall collapse. Densification strain can alternately be defined as the strain at which the tangent modulus of the stress–strain curve attains the value that corresponds to 3% of the elastic modulus and monotonously increases from that point onwards with further deformation. The data extracted from the original stress–strain curves according to this definition differ from the previous densification strain data by less than 1%.

Maiti et al. (1984) have a theoretical prediction for densification strain, ε_d, by assuming that it is reached when all the voids within cellular material are eliminated and the relative density of deformed wood, $\rho(\varepsilon)/\rho_s$, attains the value of 1, i.e., $\varepsilon_d = 1 - \rho/\rho_s$. However, this approach overestimates the present quasi-static densification strain data by as much as 15%. Since this was also the case for their experimental data they suggest that the densification strain is reached when the relative density of wood attains the value of 0.5, i.e., $\varepsilon_d = 1 - 2\rho/\rho_s$. Even though this last relation gives a good correlation with their wide range of data for various species of wood, it still does not correlate well with the quasi-static experimental data presented in Fig. 5. The best fit to the present quasi-static data for balsa wood is given by,

$$\varepsilon_d = 0.87(1 - \rho/\rho_s), \tag{2}$$

where ρ is the initial density of balsa wood and ρ_s is the density of wood cell substance. The last linear relation implies that, for the quasi-static data, densification strain occurs 13% before the theoretical prediction (Maiti et al., 1984). The packing/compaction involves the random folding and crushing of cellular elements and therefore occurs in a stochastic manner, which leads to inefficiency in packing and, thus, to the fact that its prediction is not straightforward. For dynamic data, cellular packing efficiency degrades further due to the effect of increased strain rate and for dynamic data in Fig. 5 densification strain is given by,

$$\varepsilon_d = 0.75(1 - \rho/\rho_s), \tag{3}$$

which implies a degradation of 25% over its theoretical value represented by the terms within the brackets. The difference in the degradation of packing efficiency between quasi-static and dynamic loading conditions may, of course, be qualitatively attributed to the effects of micro-inertia experienced by the cell walls during dynamic deformation. However, to quantify its contribution to the packing inefficiency again is not easy. Having discussed these observations, it is still interesting to note that, independent of the initial density of balsa wood, experimental densification strain data correspond to a constant factor (0.87 for quasi-static and 0.75 for dynamic loading) of the theoretical prediction.

It may be argued that the transverse deformation effects should also be considered in the discussion presented above since the experimental data comes from the specimens compressed under uniaxial stress conditions. Let us assume that the densification starts when the initial volume of balsa specimen (V_0) is compressed by ΔV, which is a certain factor (k) of the initial void volume (V_v). Thus, volumetric strain at this point is given by,

$$\frac{\Delta V}{V_0} = k\frac{V_v}{V_0} = k\frac{V_0 - V_s}{V_0} = k(1 - \rho/\rho_s) \tag{4a}$$

and also

$$\frac{\Delta V}{V_0} = \sum_{k=1}^{3} \varepsilon_k = \varepsilon_d(1 - \nu_{AT} - \nu_{AR}) \tag{4b}$$

where ν is the Poisson's ratio and the subscripts A, T and R stand for natural orthogonal directions in wood as described in Section 2.1. Thus,

$$\varepsilon_d = \frac{k}{1 - v_{AT} - v_{AR}}(1 - \rho/\rho_s) \tag{5}$$

in which the last term in parenthesis represents the theoretical densification strain under uniaxial strain conditions, k can be defined as the packing factor, and the denominator of the first term stands for the transverse deformation effects. The comparison of the last relation (Eq. (5)) with the Eqs. (2) and (3) justifies the usage of the term "packing efficiency" for the experimental constants 0.87 and 0.75, which correspond to the first term in Eq. (5), because any possible effect of transverse deformation should be the same for both quasi-static and dynamic loading conditions.

3.2. Energy dissipation

As has been emphasized in preceding paragraphs, plateau stress and densification strain are two important quantities that directly determine the energy dissipation capacity of the material under consideration. Even though their product gives satisfactory prediction for the specific energy dissipation capacity, in order to produce more realistic data by accounting for the elastic part of loading as well it was computed through the integration of area under stress–strain curves until densification strain and the results are presented in Fig. 6 for both unit volume and unit mass. Therefore, the data presented represent the maximum amount of energy that can be dissipated safely, i.e., by limiting maximum transmitted force to the one associated with the failure strength of balsa wood. The effect of transition in progressive deformation mode from buckling to kink band formation is apparent in Fig. 6 either in the form of plateau region (volume based data) or in the form of a dip (mass based data) in the density range of 170–200 kg/m^3. When considered together with the decrease in densification strain with density (Fig. 5), slight leveling of plateau stress (see Fig. 4(b)) during this transition results in the obvious leveling of the energy dissipated per unit volume (Fig. 6). The effect of increasing density in this plateau region can be seen as a transient drop in the energy dissipated per unit mass. As a whole the energy dissipation capacity of balsa wood lies between 30 and 90 kJ/kg, which is comparable or better than the most fiber reinforced composite tubes. Mamalis et al. (1997) reports in their review for the crashworthiness capability of composite material structures that specific energy dissipation/absorption capacities of fiber reinforced hallow tubes made of carbon/epoxy, aramid/epoxy, glass/epoxy and carbon/PEEK lie between 50–99, 9–60, 30–53 and 127–180 kJ/kg respectively, variations arising mostly from the fiber orientation angle and stacking sequence. Actually balsa wood owes its remarkable energy dissipation capacity to its naturally tailored microstructural features

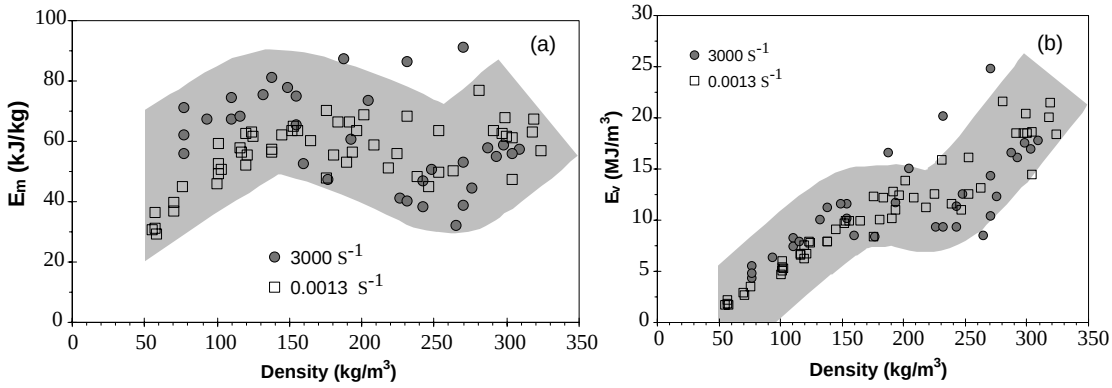

Fig. 6. Variation in the specific energy absorption capacity of balsa wood with density and strain rate.

such as the tubular honeycomb geometry of its cells and the fine nano-architecture and composite nature of its cell walls.

Fig. 6 also shows the effect of elevated strain rate on the energy dissipation capacity. Even though there appears a slight increase in dynamic data for low densities it is highly scattered and intermixed with the quasi-static data for higher densities. Once again this phenomenon is attributed to the transition in deformation mode and, thus, to the increased effect of random stress perturbations on the plateau stress level for high densities. For low-density balsa wood, the cells deform by buckling. Since the length scale of local deformation is limited to the length of buckles, which is much smaller than that in kink banding mode, stress perturbations are also small and therefore perturbation based softening is slightly suppressed by the micro-inertia based hardening, resulting in a slight increase in the plateau stress for low density balsa wood (see also Fig. 4(b)). This rationale is also consistent with the experimental observations that plateau stress of aluminum honeycombs with low relative density tends to increase with the rate of loading when the deformation mode is buckling (Goldsmith and Sackman, 1992; Wu and Jiang, 1997; Zhao and Gary, 1998; Harrigan et al., 1999). However, with the transition in deformation mode for higher density balsa wood, the length scale involved becomes larger and, therefore, induces higher stress perturbations which, in turn, both suppress the inertial effects and result in a wider scatter.

3.3. Failure modes

Vural and Ravichandran (2003) report that buckling and kink band formation are two major failure modes for low-density and high-density balsa wood, respectively, under quasi-static loading conditions, the transition density being given in the range 170–200 kg/m^3. In order to reveal microstructural failure modes under dynamic loading conditions, the balsa specimens are compressed at high-strain-rates to predetermined strains by using stop-rings and then carefully sectioned to perform SEM examination on the failure surfaces. The SEM observations on recovered specimens from both quasi-static and dynamic tests clearly show that the failure mode undergoes transition from elastic/plastic buckling of cell walls to kink band formation as the density of the material increases. The micrographs of two specimens showing the typical dynamic deformation mode in low- and high-density balsa wood are presented in Fig. 7. The rate of loading does not change the deformation mode. Similar micrographs for quasi-statically loaded specimens can be found in Vural and Ravichandran (2003).

The major mechanism during both initial failure and progressive deformation is micro-buckling for low-density balsa wood, density below 170 kg/m^3. When the specimen density is beyond 170–200 kg/m^3 range, thickness to diameter ratio of tubular cells increases and the critical stress for buckling becomes too high so that another mechanism (kink band formation) starts operating. Initiation of this new deformation mode is sensitive to and triggered by initial fiber (cell, grain) misalignments which are naturally present in the microstructure (Fig. 1(b)). Therefore, the appearance of kink band formation in denser specimens is attributed to the increase in fiber misalignments caused by the thicker ray cells penetrating the entire microstructure in radial direction. Vural and Ravichandran (2003) report the experimental evidence of larger fiber misalignments in denser balsa wood as well as analytic models that explain the transition in failure modes.

4. Models for inertial stress enhancement

4.1. Background

It is well known that the strength enhancement observed in materials/structures under dynamic loading conditions is attributed to one or both of the two factors which are not present in quasi-static loading:

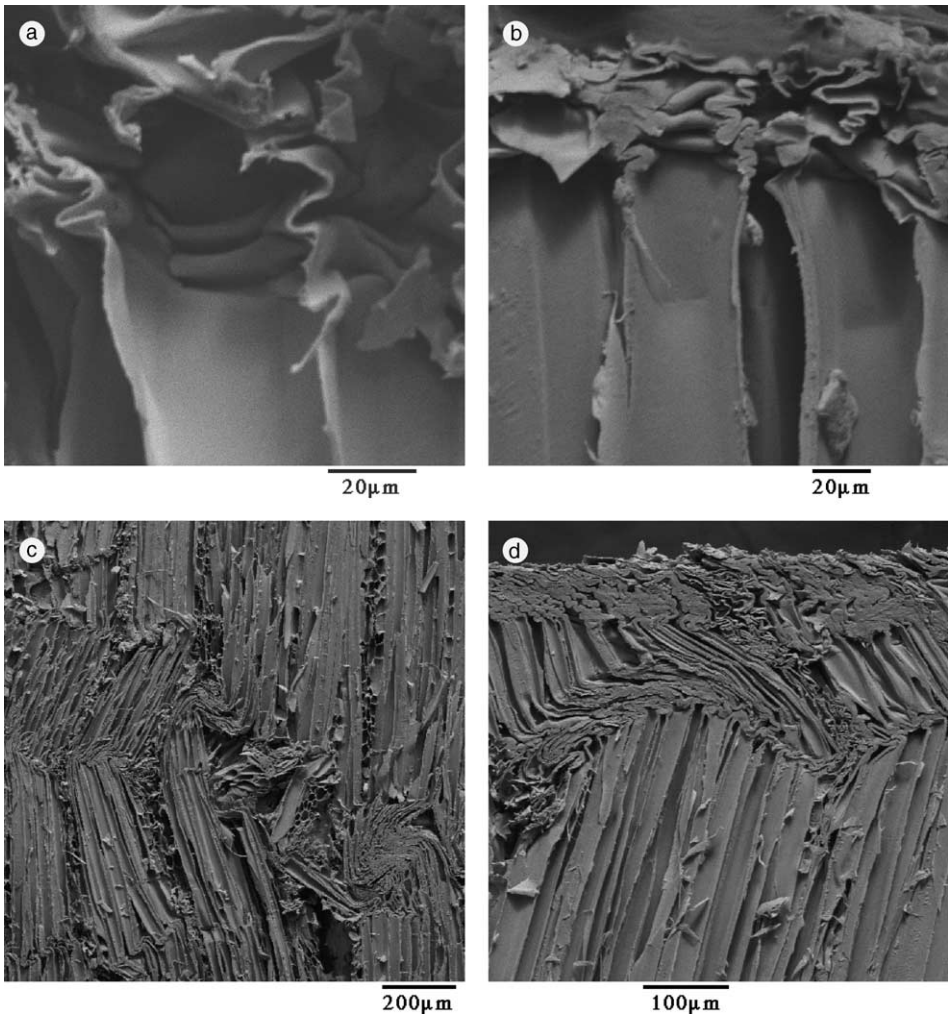

Fig. 7. Scanning electron micrographs of recovered specimens after dynamic compression: (a) and (b) deformation occurs in buckling mode for low-density balsa wood (total strain = 0.07, $\rho = 88$ kg/m^3, $\dot{\varepsilon} = 3200$ s^{-1}); (c) and (d) kink band formation in denser specimens (total strain = 0.09, $\rho = 293$ kg/m^3, $\dot{\varepsilon} = 3000$ s^{-1}).

(i) strain-rate sensitivity of material properties and (ii) inertial forces. The inelastic behavior of cellular solids is governed mainly by the progressive deformation mechanisms which are strongly controlled by the cellular geometry of the structure. Studies on the dynamic response of cellular solids that are made of strain-rate insensitive materials show that, while the materials with periodic topology (e.g., aluminum honeycombs) are prone to dynamic strength enhancement in longitudinal direction (Goldsmith and Sackman, 1992; Wu and Jiang, 1997; Zhao and Gary, 1998; Baker et al., 1998; Harrigan et al., 1999), those with stochastic topology (e.g., aluminum foams) are insensitive to the rate of loading (Ashby et al., 2000; Deshpande and Fleck, 2000), suggesting that there exists a close relationship between the cellular topology and inertial dynamic strength enhancement. It should be noted that due to the anisotropy of materials with periodic topology their response to dynamic loading might vary depending on the loading direction. In fact, an argument of this type can also be related to a series of studies on what is called type I and type II structures (Calladine and English, 1984; Zhang and Yu, 1989; Tam and Calladine, 1991; Su et al., 1995a,b;

Karagiozova and Jones, 1995), which have succeeded in explaining certain anomalies regarding their energy absorbing capabilities under dynamic loading conditions. Those studies, in the simplest terms, discuss that the structures with an "unstably softening" quasi-static load–deflection curve (type II) are much more susceptible to inertia based dynamic strength enhancement than the structures with a "flat topped" load–deflection curve (type I). Within this terminology, the mechanical response of type I structures are characterized by that of circular tubes under transverse loading in which the bending mode of collapse defines the deformation for both quasi-static and dynamic loading conditions. However, type II structures are represented by longitudinal struts/plates that undergo bending deformation around localized hinges and, as explained theoretically by Su et al. (1995a,b), under dynamic loading conditions lateral inertia forces induce an initial phase of axial compression in the struts which results in dynamic stress enhancement before the bending mechanism is recovered. Thus, within this framework, mechanical response of honeycomb materials in longitudinal direction is reminiscent of type II structures while the response of foams and honeycombs in transverse direction falls into the category of type I structures. This analogy is also supported by the experimental data in the references given above. However, there are two important points that need to be discussed. First, the deformation in cellular materials mostly occurs in localized bands and, therefore, actual strain rates experienced by the localized regions may be an order of magnitude higher than the nominal strain rate applied over the cellular material. This situation requires defining a realistic characteristic length scale to account for localization effects. Second, the term dynamic covers a wide range of impact velocities (or strain rates) and depending on its magnitude the role of inertia should be evaluated in two subcategories: (i) up to a critical impact velocity, *lateral inertia* (or *micro-inertia*) is effective in stress enhancement and its effect on dynamic strength enhancement is limited by the constitutive response of the material that make up the cellular solid, it is this inertia that is responsible for the dynamic strength enhancement observed in type II structures, (ii) for higher impact velocities, *axial inertia* that is associated with the propagation of shock waves through the cellular structure is effective in stress enhancement and it may dominate the dynamic strength enhancement well above the constitutive capacity of material, this type of inertia may result in dynamic strength enhancement in both type I and type II structures.

Reid and Peng (1997) developed a structural shock wave model and compared its strength predictions with experimental data for wood, which is impacted at velocities in the range from 30 to 300 m/s. The strength enhancement in transversely loaded specimens follows the predictions of their shock model, both increasing substantially with increasing impact velocity. However, the predictions of shock model underestimate the dynamic strength of balsa wood in longitudinal direction for the range of impact velocities they used. They also calculate a critical impact velocity for longitudinal loading above which the deformation will proceed in a shock-like manner and give its value as 360 m/s. Thus, their test velocities lie in a range where the shock wave effects are not expected. Almost all of their data show a dynamic strength enhancement factor in the range 1.5–2.3, the latter factor corresponding to the yield stress of wood cell material. They attribute this strength enhancement to micro-inertial effects at the cellular scale by noting the upper bound of 2.3. Even though the literature on the dynamic behavior of cellular materials often refers to the micro-inertia for qualitative explanations of the rate effects observed, an attempt to quantify its effects has not been undertaken yet, which will be the subject of following sections.

The post-mortem SEM investigations of the present study on compression loaded balsa wood specimens reveal that the deformation mechanisms operating at the microstructural level are either *buckling* or *kink band formation*, depending mainly on the density of wood. Increasing the strain rate does not change these primary deformation mechanisms. However, compressive strength of balsa wood experiences a substantial increase when loaded at high-strain-rates (see Fig. 4(a)). Since the deformation in cellular structures is associated with the large displacements of microstructural elements that make up the cellular solid, these elements experience rapid acceleration under dynamic loading. Therefore, it is not unreasonable to expect that the inertial forces predominate the dynamic response of balsa wood. With this reasoning, and also due to the lack of experimental data for the strain-rate sensitivity of wood cell material (not wood as a whole),

the effect of micro-inertia is investigated to quantify its contribution to the dynamic strength enhancement. Based on the kinematics of deformation mode, simple models for buckling and kink band formation are discussed in the following sections.

4.2. Buckling

The present analysis is essentially based on the recognition of the subsequent deformation phases that are shown schematically in Fig. 8. The initial configuration of balsa wood is illustrated in Fig. 8(a) in which the vertical lines represent the longitudinal cell walls. The cell walls are assumed to have an initial imperfection in the form of a misalignment distribution though it is not demonstrated in the figure explicitly. The first phase (I) of dynamic loading is governed by the homogeneous elastic deformation of the cell walls until a critical stress level, which is the quasi-static strength of material, is reached. The second phase (II) represents the initiation of buckling instability and elasto-plastic hinge formation within localized regions. In this phase, lateral inertia comes into play and, contrary to quasi-static process, raises the stress level within cell walls by resisting the transverse motion and, thus, inducing further compression along the cell walls. Therefore, it is this phase that contributes to the dynamic strength enhancement. The third phase (III), which corresponds mainly to the plateau region in a typical stress–strain curve (see Fig. 3), is characterized by further deformation within localized regions by bending at plastic hinges and the formation of new localization sites.

As it is evident from the preceding discussion, the effect of transverse inertia on the dynamic strength enhancement is analyzed by modeling the initiation of buckling instability in phase II shown in Fig. 8. Fig. 9 shows the idealized geometry of a half-buckle, (a) in its initial condition and (b) at a typical stage after the initiation of the buckling instability. For the sake of simplicity, the segments of cell walls that buckle are idealized as two axially deformable light rods with lumped masses at each end of the rods. It is further assumed that the two rods are freely hinged to each other at the central node. In Fig. 9(a) the initial misalignment angle is θ_0 and the overall length of the initial buckle is l, while in Fig. 9(b) the current angle is θ and the overall current length is $l-u$, where u is the shortening of the length of the cell wall due to elastic/plastic deformation. Between Fig. 9(a) and (b), the vertical height of the half-buckle is correspondingly reduced by y, which is computed geometrically, as follows:

$$y = l\cos\theta_0 - (l-u)\cos\theta. \tag{6}$$

By assuming that the angle θ remains small during phase II, the truncated Taylor series expansion gives,

$$\cos\theta = 1 - \theta^2/2 + \cdots \tag{7}$$

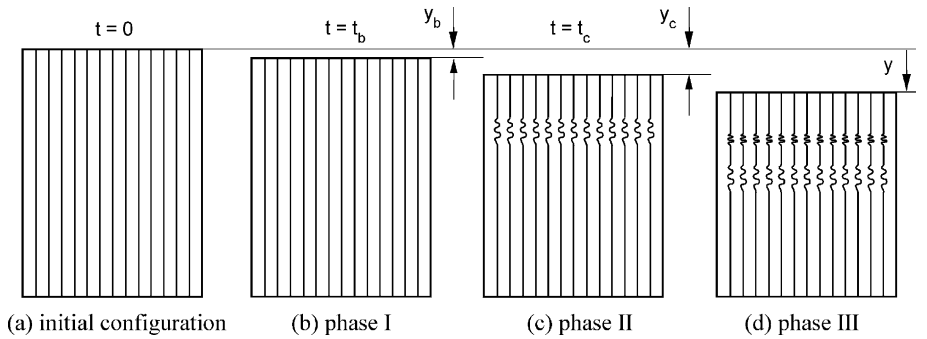

Fig. 8. Subsequent phases of deformation: (a) initial configuration of cellular structure, (b) homogeneous elastic loading, (c) initiation of localized buckling deformation and (d) progressive deformation through localized regions.

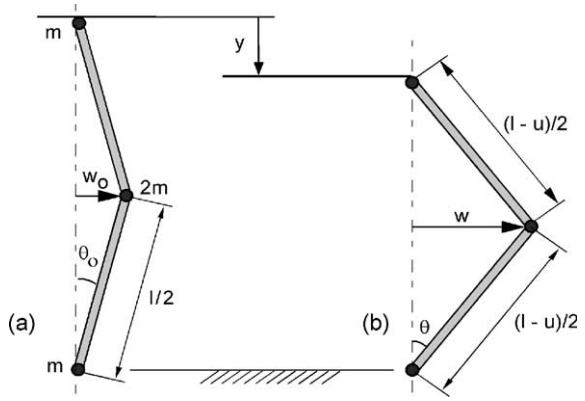

Fig. 9. Idealization of half-buckle geometry to bars and lumped masses: (a) original configuration with initial cell wall imperfection and (b) deformed configuration showing the definitions of angles (θ), transverse displacement (w), vertical shortening (y) and axial shortening (u).

and the transverse displacement w and angle θ can be related by,

$$w = \theta l/2. \tag{8}$$

Hence, after neglecting the higher-order terms, the vertical shortening of the half-buckle becomes,

$$y = (2/l)(w^2 - w_0^2) + u. \tag{9}$$

The rate of vertical shortening of the cell wall segment can be obtained by differentiating Eq. (9) with respect to time,

$$\dot{y} = (4/l)w\dot{w} + \dot{u} = V^* + \dot{u}, \tag{10}$$

where

$$V^* = (4/l)w\dot{w}. \tag{11}$$

The first term on the right hand side of Eq. (10) gives the vertical shortening rate, V^*, which the half-buckle would have in terms of w and $\dot{w}$, if the cell walls were *inextensional*, while the second term is the additive contribution to the total shortening rate, $\dot{y}$, due to the lengthwise elastic/plastic compression of cell walls.

At the beginning of phase II, the cell walls are already subject to a critical stress, σ_{qs}, which is the quasi-static strength of the cellular material and a known quantity due to the availability of experimental data as well as analytical predictions (Vural and Ravichandran, 2003). Therefore, in phase II, the stress in the cell walls is,

$$\sigma = \left\{ \begin{array}{ll} \sigma_{qs} + \dfrac{Eu}{l}, & u < u^*, \\ \sigma_y, & u \geqslant u^*, \end{array} \right\} \tag{12}$$

where $u^* = l(\sigma_y - \sigma_{qs})/E$, σ_y and E are the yield stress and Young's modulus of the wood cell material respectively ($\sigma_y = 350$ MPa from Cave, 1969; $E = 35$ GPa from Cave, 1968). There is an axial force of $A\sigma$ on each of the inclined cell walls and these exert a lateral force on the lumped mass at the central node, which in turn provides the lateral acceleration. Hence, the equation of transverse motion for the half-buckle can be written as,

$$\ddot{w} = \frac{2A}{lm}\sigma w, \tag{13}$$

where $A = bt_c$ (cross-sectional area of the cell wall or in this case of the rod), $m = (1/4)\rho_s lbt_c$, ρ_s is the density of solid wood cell substance which is generally taken to be approximately 1500 kg/m^3 (Wangaard, 1950; Mark, 1967), b and t_c are the width and the thickness of the cell wall respectively. Now, assuming that the vertical shortening occurs at a constant rate $\dot{y} = V_0^*$,

$$y = V_0^* t. \tag{14}$$

When coupled with Eqs. (9), (12) and (14), Eq. (13) takes the form,

$$\ddot{w} = \begin{cases} r_1 wt + r_2 w + r_3 w^3, & u < u^*, \\ r_4 w, & u \geqslant u^*, \end{cases} \tag{15}$$

where

$$r_1 = lV_0^* k, \quad r_2 = (2w_0^2 + \sigma_{qs} l^2/E)k, \quad r_3 = -2k, \quad k = \frac{8E}{\rho_s l^4} \quad r_4 = \frac{8\sigma_y}{\rho_s l^2}. \tag{16}$$

The first part of Eq. (15) corresponds to elastic compression of cell walls. This is a second-order non-linear ordinary differential equation and can be solved numerically to yield w and $\dot{w}$ with the initial conditions,

$$w = w_0, \quad \dot{w} = 0 \quad \text{at } t = 0. \tag{17}$$

If the condition $u = u^*$ is reached at a time $t = t^*$ during the phase II, the second part of Eq. (15) corresponds to plastic yielding of cell walls and can be solved analytically with the initial conditions,

$$w = w^*, \quad \dot{w} = \dot{w}^* \quad \text{at } t = t^* \tag{18}$$

to give,

$$w = w^* \cosh(\sqrt{r_4}(t - t^*)) + \dot{w}^* \sinh(\sqrt{r_4}(t - t^*)). \tag{19}$$

Fig. 10 shows the typical plots of $\dot{y}$, V^* and σ as a function of time, t. The upward concave curve is for V^*, and the horizontal straight line is for $\dot{y}$. The vertical intercept between the two curves is equal to $\dot{u}$, by virtue of Eq. (10). Furthermore, since $\dot{u} \geqslant 0$ by hypothesis (as the cell walls are assumed to be deforming in compression), the solution ceases to be valid beyond the time $t = t_1$ at which the two curves intersect. Thus, the intersection of the two curves marks the end of the phase II and the beginning of the phase III, i.e., the phase in which further deformation occurs only by the rotation of the elasto-plastic hinges and the formation of subsequent buckling (localization) sites. Fig. 10 also shows the evolution of the stress experienced by the cell walls. As can be seen, under dynamic loading conditions the stress may be significantly raised over its quasi-static critical value due to the lateral resistance offered to the cell walls by transverse inertia.

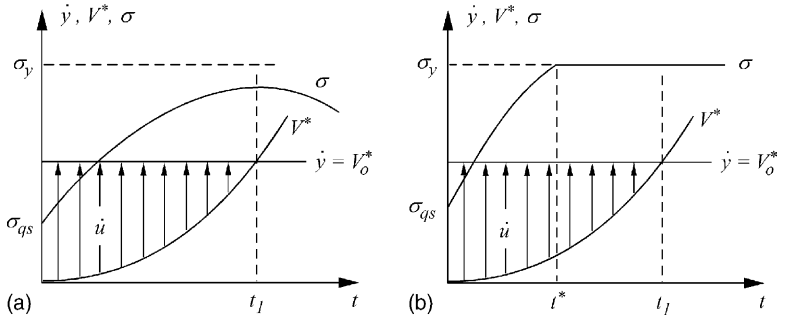

Fig. 10. Typical plots for the evolution of vertical shortening rate $\dot{y}$, $V^* = (4/l)w\dot{w}$ axial shortening rate $\dot{u}$ and the cell wall stress $\sigma = \sigma_{qs} + Eu/l$ with time during the phase II. (a) When the axial shortening occurs only by elastic compression and (b) when the yield stress is reached.

At the end of phase II, as the transverse displacement rate reaches a critical value, axial shortening rate in the cell walls becomes zero so that further vertical shortening can be accommodated only by the rotation of hinges. This situation results in a peak in the stress–strain response of the material, which is followed by a more complex behavior. The present analysis assumes, for the sake of simplicity and to focus on the effect of inertia, that the hinges are free to rotate. However, actual situation involves the formation of an elasto-plastic hinge that resists the rotation. The complexity arises from the fact that, beyond the critical point, as the inertia does not support the development of further compression, and hence the stress enhancement, along the cell walls, but, on the contrary, favors the partial unloading, the moment at the hinges takes over the role to support the cell wall stress. Depending on the competition between these two opposing effects the overall flow stress of the material may experience a sudden drop or mildly level off. The peak stress, transverse displacement and the cell wall thickness are among the important factors that affect the evolution of this competition. The evolution of stress response beyond the peak stress, i.e., after phase II, is not pursued in the present analysis.

4.2.1. Model parameters

In order to predict the dynamic strength of balsa wood, the model developed above needs several inputs regarding the material properties, initial cell wall imperfections and characteristic length of localization, which will be discussed next. Vural and Ravichandran (2003) reported the quasi-static strength of balsa wood as a function of its density over its entire density range. A linear fit to their experimental data for quasi-static strength in MPa gives,

$$\sigma_{qs}^{\infty} = 0.131\rho - 5.23, \tag{20}$$

where ρ is the density of the cellular material, i.e., balsa wood, in kg/m^3. Note that Eq. (20) is valid for the density, ρ, in the range of 55–380 kg/m^3. Thus, the corresponding stress experienced by the individual cell walls at the time of quasi-static collapse can be calculated as,

$$\sigma_{qs} = (\rho_s/\rho)\sigma_{qs}^{\infty}. \tag{21}$$

The SEM observations on deformed low-density balsa specimens suggest that the half-buckle length of cell walls (l) is roughly equal to the cell width (b) (see Fig. 7(a) and (b)). This is also further supported by the elastic buckling analysis of thin plates. Therefore, half-buckle length (l) that is shown in Fig. 9 is taken as 30 μm and the misalignment angle θ_0 has been chosen as 1°. Finally, the vertical shortening rate of half-buckles (V_0^*) should be provided to the model as the boundary condition. Given the specimen length (L_s) and the strain rate ($\dot{\varepsilon}$), the overall shortening rate of specimen (V_0) can be easily calculated by

$$V_0 = \dot{\varepsilon}L_s. \tag{22}$$

However, a characteristic length scale (l_c) for the localization is still needed in order to have a reasonable vertical shortening rate for half-buckles. The SEM observations on buckled specimens suggest that the characteristic length of localization region is on the order of 200 μm. This magnitude for the length scale is also supported by the fact that hexagonal balsa cells are generally divided into smaller prismatic boxes by one or two lateral support membranes along their length. Easterling et al. (1982) and Gibson and Ashby (1997) report the length of these smaller cellular elements as being in the range 175–285 μm, which will be used as the lower and upper bounds for the characteristic localization length, l_c. Thus, the vertical shortening rate for half-buckles can be determined,

$$\dot{y} = V_0^* = \dot{\varepsilon}L_s l/l_c. \tag{23}$$

Since the present experiments are performed at a nominal strain rate of $\dot{\varepsilon} = 3000\ s^{-1}$, and with a specimen length (L_s) of 5 mm, the range of 1.6–2.6 m/s will be used for the vertical shortening rate of half-buckles.

Based on the model parameters introduced above for balsa wood, the dynamic strength predictions of the model are discussed and compared with the experimental results in the next section.

4.3. Kink band formation

As already has been discussed in previous sections, kink band formation is the major failure mode for high-density balsa wood. The basic approach adopted for the above analysis will be preserved also here, which states that the initiation of localized deformation, i.e., kink band formation, occurs after the homogeneous elastic deformation when the quasi-static strength of material is reached. Therefore, the analysis will focus on the phase II where the inertial forces are dominant. Based on experimental observations, Fig. 11 schematically shows the various combinations of kink band formation within cellular composites, e.g., balsa wood. Basically they can be divided into two subcategories: *single kink* band formation and *conjugate kink* band formation. Fig. 12 shows the idealized geometry of these kink bands that will be employed for the analysis of inertial effects. Eq. (6)–(12) and (14) pertaining the kinematics are also valid for kink band analysis if the definitions of Fig. 12 are adopted regarding the geometry and mass for the kink band. The equations of motion in the transverse direction are given by,

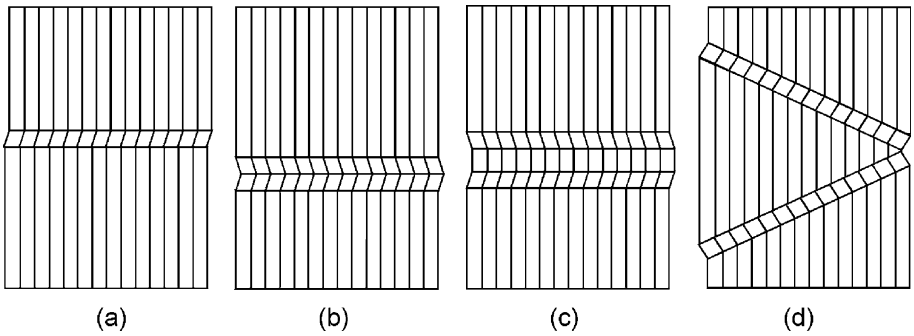

Fig. 11. Various combinations of kink band formation: (a) single kink band, (b) conjugate kink bands, (c) and (d) conjugate kink band formation with added mass.

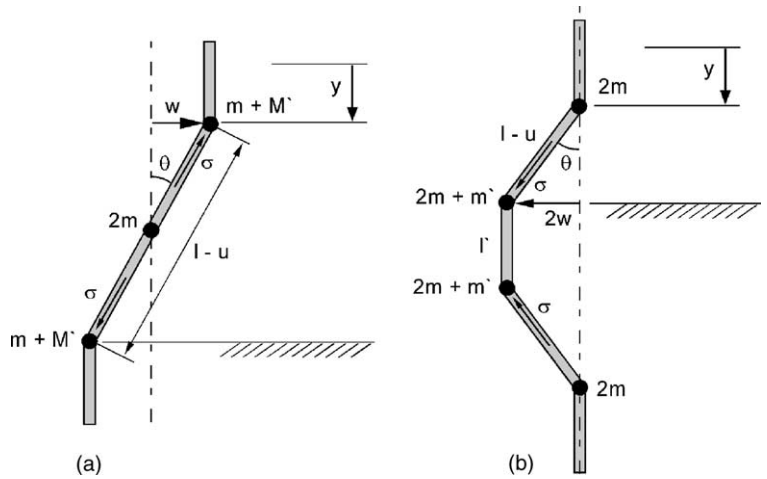

Fig. 12. Details of idealized kink band geometries: (a) single kink band and (b) conjugate kink bands with added mass.

$$\ddot{w} = \frac{2A}{l(m + M')}\sigma w \tag{24a}$$

for a single kink band, and by,

$$\ddot{w} = \frac{A}{l(2m + m')}\sigma w \tag{24b}$$

for conjugate kink band geometries where $M' = (1/2)(L_s - l)bt_c\rho_s$ stands for half the mass of specimen outside the single kink band, and $m' = (1/2)l'bt_c\rho_s$ for the added mass that is accelerated between the conjugate kinks. Using Eqs. (9), (12) and (14), the equations of motion for the single kink and conjugate kink band configurations take exactly the same the form as Eqs. (15) and (19) with the coefficients r_i $(i = 1, 4)$ replaced by r_i' and r_i'', respectively, which is given by,

$$r_i' = r_i\frac{k'}{k} \quad (i = 1, 4) \quad \text{and} \quad k' = k\left(\frac{l}{2L_s - l}\right) \quad \text{for single kink band,} \tag{25a}$$

$$r_i'' = r_i\frac{k''}{k} \quad (i = 1, 4) \quad \text{and} \quad k'' = k\left(\frac{l}{4(l + l')}\right) \quad \text{for conjugate kink band,} \tag{25b}$$

where r_i and k are given by Eq. (16). Thus, the differential equations governing the transverse motion of system are of the same character for both buckling and single/conjugate kink band formation. Therefore, the previous discussion on Fig. 10 regarding the evolution of velocity components and the cell wall stress during phase II is also valid for kink band formation mode.

4.3.1. Model parameters

The critical level of nominal stress at the beginning of kink band instability is given by Eq. (20) because it defines the quasi-static strength of balsa wood over its entire density range. Therefore, it will be used in conjunction with Eq. (21) to obtain the critical cell wall stress (σ_{qs}).

Experimental evidence shows that the width of kink band (l) may vary from 100 μm to as much as cell length, which is approximately 650 μm. As will be discussed in detail in the next section, the dynamic strength prediction of the model is independent of the kink band width (l) when the added masses (m' and M') are ignored or when they are a certain fraction of kink band mass ($4m$). However, when the added mass is kept constant, the smaller the kink band width, the higher is the dynamic stress enhancement.

The initial misalignment angle for the kink band formation is much larger than that is assumed for buckling because in kink band mode it represents the misalignment of longitudinal cells as a whole while in buckling mode initial misalignment is a measure of waviness within the cell walls. Based on the SEM observations, Vural and Ravichandran (2003) used $\theta_0 = 9°$ as an average misalignment angle in their analysis to predict the critical stress for quasi-static kink band formation in balsa wood. The same value of initial misalignment angle will be used for the dynamic analysis as well.

The characteristic length of localization is the same as kink band width for single kink mode ($l_c = l$) and twice the width of kink band for conjugate kink mode ($l_c = 2l$). Therefore, in conjunction with Eqs. (22) and (23), the vertical shortening rate ($\dot{y}$) for single kink and conjugate kink band configurations shown in Fig. 12 is computed to be 15 and 7.5 m/s, respectively.

5. Comparison of model with experiment

Before making the direct comparison between the model predictions and the experimental results, it is helpful to discuss the essential features pertaining to the buckling and the kink band models. The basic

parameter common to both the models is the term σ_{qs}, which represents the state of stress within the individual cell walls at the initiation phase of buckling or kink band instability. Independent of the failure mode, this critical stress level is obtained using the Eqs. (20) and (21). However, it should be noted that it is not a constant but varies as a function of the density of entire cellular structure, i.e., balsa wood.

In a naturally occurring material such as balsa wood it is inevitable to have geometric material imperfections at different length scales within the cellular structure. Thus, the second parameter, initial misalignment angle θ_0, represents the measure of this geometric imperfection. For buckling model, it defines the extent of waviness along the cell walls and is assumed to be 1° for present predictions. For kink band model, misalignment angle stands for the geometric imperfection at a larger length scale that is comparable with the cell length. Experimental evidence shows that there exist fiber (cell) misalignments in balsa wood and they vary in the range 7–11°, particularly on LT plane due to the presence of ray cells. Therefore, an average value of 9° is adopted for the kink band model, which is also consistent with the value used in quasi-static kink band model for balsa wood (Vural and Ravichandran, 2003).

In buckling model, the dynamic strength prediction depends on the buckling wavelength only through the characteristic length of localization (l_c). These two quantities together determine, through Eq. (23), the vertical shortening rate of half-buckles, which in turn forms the boundary condition for half-buckle configuration. If this velocity boundary condition is kept constant, even though the coefficients in the equation of motion (Eq. (15)) are functions of the half-buckle length, the strength prediction of the model becomes independent of the buckling wavelength. Since the half-buckle length is chosen to be 30 μm, which is both supported by SEM observations and consistent with the theoretical elastic buckling analysis of thin plates, lower and upper bounds for the characteristic length of localization (175–285 μm) set the upper and lower limits, respectively, for the dynamic strength prediction in buckling mode. As shown in Fig. 13, experimental data are in quite good agreement with these limits.

In the kink band model, it is recognized that the part of material outside the localization band may also be accelerated and the lateral inertia of this added mass has a contribution to the dynamic stress enhancement. In single kink band configuration this is accounted by the term M', which is half the mass of specimen outside the kink band. This mechanism involves the acceleration of large specimen masses below and above the kink band in opposite directions and, therefore, the stress exerted to cell walls due to lateral inertia reaches the yield stress of the wood substance well within the phase II (Fig. 10(b)), resulting in a dynamic strength enhancement restricted by the plastic collapse of cell walls. This situation occurs irrespective of the choice of kink band width ($100 < l < 650$ μm). The acceleration of the entire specimen mass

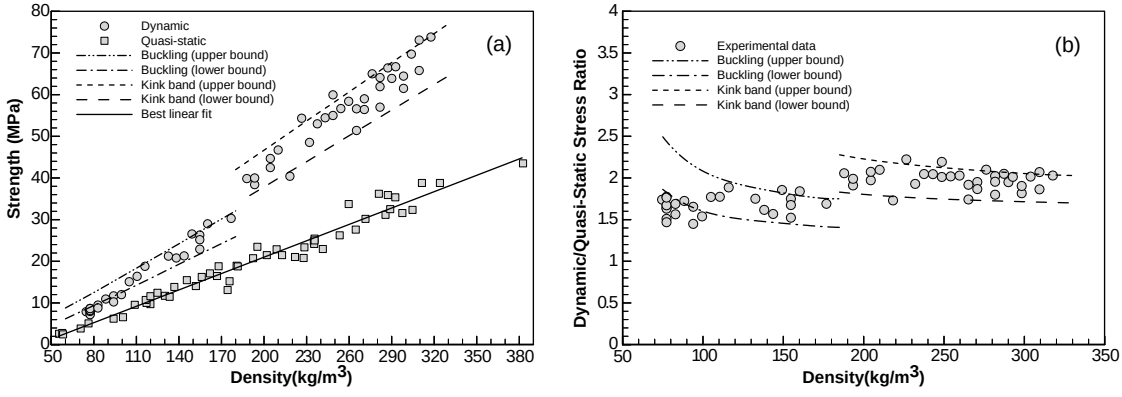

Fig. 13. Variation of dynamic and quasi-static compressive strength with density for balsa wood: experimental data versus model predictions.

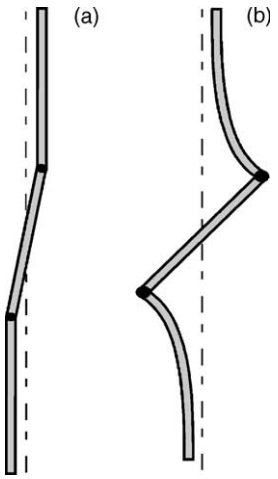

Fig. 14. Schematic geometry of deformation that accounts for cell wall bending.

may be thought to be irrelevant in actual single kink band formation process and instead a deformation geometry that accounts for the bending of cell walls (see Fig. 14) may be considered more appropriate. In this case, the total effective mass accelerated at the tips of kink band will be restricted to a certain factor of kink band mass, which can be as small as the kink band mass itself under the most conservative assumption. Even in this situation that corresponds to single buckle formation, the lateral inertia is found strong enough to induce the yield stress along the cell walls. Therefore, for the current material and model parameters, single kink model produces an upper bound for the compressive strength prediction, which is given by the plastic collapse stress of entire cellular structure. This upper bound is plotted in Fig. 13.

On the other hand, the conjugate kink band model represents a unique deformation mode in which the material finds a way out to avoid the large accelerations. When the added mass accelerated between the conjugate kinks ($m' \propto l'$) is assumed not to exist, the model gives the lower bound for the dynamic strength of balsa wood as is shown in Fig. 13. If the length of accelerated region is chosen to be 70% of the kink band width, i.e., if $l' = 0.7l$, the lateral inertia becomes strong enough to exert the yield stress along the cell walls so that the upper bound of plastic collapse is attained. Thus, depending on the added mass, the predictions of the conjugate kink model covers the entire range between lower and upper bounds plotted in Fig. 13.

Even though the buckling and kink band models developed in the preceding section are physically based on experimental observations, significant simplifications such as the lumped masses and the neglect of cell wall bending and plastic hinge formation are introduced in order to keep the evolution of inertial forces tractable. However, it should be noted that the present analysis attempts to cover only the initiation phase of buckling and kink band instability, where the inertial forces are the most effective and there is very limited hinge rotation and cell wall bending, rather than the entire progressive deformation process which involves substantial hinge rotation and subsequent localizations in the neighboring sites. As shown in Fig. 13, the upper and lower bound predictions of these simplified models are in quite good agreement with the experimental dynamic strength data. This agreement suggests that the dynamic strength enhancement in balsa wood is dominated by the transverse inertia of the elements that makes up the cellular structure. Even though the present study on balsa specimens shows that the significant amount of dynamic strength enhancement can be well explained by cellular micro-inertia, the question on the possible role of viscous effects still needs to be addressed. One way to do this is to conduct high-strain-rate experiments on isolated cell wall material, which is extremely challenging. Another way may be to test the strain-rate sensitivity of specimens that will be machined out of balsa specimens compressed up to their densification strain or even

further. However, the latter method will bring about new questions arising from the anisotropy of cell wall material because the direction of loading for densified balsa specimens will not be along the cell walls. The investigation of viscous effects and its contribution to the dynamic strength enhancement in balsa wood deserves further study.

On the other hand, for the range of strain rates investigated (10^{-3}–10^{3} s^{-1}), the present experimental data (Fig. 4) shows that the plateau stress is relatively insensitive to the variation in strain rate while the compressive strength (peak stress) exhibits significant sensitivity. Since the progressive deformation in the plateau region is mainly characterized by the intensive localized plastic deformation at around the hinges and the transverse inertia is negligible at this phase of deformation, experimental data indirectly suggest that the contribution of viscous effects to the dynamic strength enhancement should be insignificant as compared to that of inertial effects. It should be noted that the deformation mechanisms and the interactions in the plateau region is quite complex and, therefore, this indirect suggestion needs to be further investigated.

Another issue is that the balsa wood is composed of different kinds of cells and, therefore, the applicability of the present models should be addressed under the concerns about the homogeneity of cell types. Apart from the homogeneously distributed diffuse sap channels, balsa wood has two structurally important cell types: (i) long prismatic hexagonal cells (grains) and (ii) shorter brick-shaped ray cells (see Fig. 1). The groups of ray cells are continuous along the radial direction but they are discontinuous and have a finite depth in the longitudinal direction. The models developed to quantify micro-inertia induced strength enhancement for buckling and kink band formation modes are essentially based on the kinematics of deformation during localized failure initiation. Therefore, the issue of homogeneity in cell types should be considered in terms of its effect on the kinematics of deformation at microscale. The SEM studies on recovered specimens reveal that the buckling wavelength in the walls of ray cells tends to be the same as that in grains. In the case of kink band formation, the length scale of deformation is much larger and the groups of ray cells displace exactly in the same manner as the grains. Thus, independent of the mass ratio of ray cells to grains in a balsa specimen, the contribution of ray cells to micro-inertial hardening should be expected to be the same as grains. In other words, as long as the kinematics of deformation is not altered due to the inhomogeneous distribution of cell types, which is the experimentally observed situation for balsa wood, the models should be considered applicable for wood structure.

Based on the results of present analysis, it should be pointed out that the micro-inertia of the elements in cellular materials may play an important role in the strength enhancement of these materials under dynamic loading conditions.

6. Conclusions

High-strain-rate mechanical properties of a naturally occurring cellular material, balsa wood, have been investigated experimentally over its entire density spectrum from 55 to 380 kg/m^3. The dynamic results regarding the compressive strength, plateau stress, densification strain and energy dissipation capacity have been discussed and documented, and compared with the quasi-static results reported previously (Vural and Ravichandran, 2003). It has been demonstrated that initial failure strength of balsa wood is very sensitive to the rate of loading (50–130% increase over corresponding quasi-static values) while plateau stress remains unaffected by the strain rate. This difference in response to increasing strain rate is explained in terms of the differences in the kinematics of deformation, associated micro-inertia and the level of stress perturbations during initial failure and progressive deformation. The packing efficiency of balsa wood, as manifested by the densification strain, has been found to degrade with the rate of deformation. As in quasi-static loading, buckling and kink band formation were identified to be two major failure modes in dynamic loading as well. Kinematics of deformation of the observed failure modes and associated micro-inertial effects has

been modeled and discussed to explain measured dynamic strength enhancement. The predictions of model show that the micro-inertia of cellular elements may result in strength enhancement up to the constitutive bounds of cell wall material. Specific energy dissipation capacity of balsa wood was analyzed and determined to be comparable with those of fiber-reinforced polymer composites.

As opposed to the bulk materials, the localized deformation in cellular solids is associated with large local displacements mainly due to the discrete nature of cellular topology, which leads to large accelerations in cellular elements under dynamic loading conditions. The modeling effort introduced in the present study seeks to understand and quantify the role of these cellular accelerations (micro-inertia) on experimentally observed dynamic strength enhancement. As has been elaborated in the preceding sections the governing physics for micro-inertial strength enhancement leads to further compression of cell walls due to the non-zero component of transverse inertial forces along the cell walls. Therefore, the models introduced in the present study focus on the quantification of these resolved inertial forces irrespective of the complexity of kinematics associated with failure. It should be underlined that the kinematics of failure is 3D in buckling mode, while it is 2D in kink band formation mode mainly because high anisotropy of balsa wood in its transverse plane forces the failure to occur in LT plane. However, the 3D or 2D character of failure kinematics loses its importance in this particular problem since the dynamic strength enhancement is essentially driven by transverse inertia. Thus, the distinction between transverse directions is not critical and a realistic representation of 2D failure kinematics as applied here is sufficient as long as one aims at capturing the governing physics with reasonable simplicity. From this perspective, the present models are based on 2D representation of experimentally observed failure kinematics and keep track of resolved inertial forces along the cell walls. With these features the models attempts to provide a tool to understand and quantify the effect of cellular micro-inertia at intermediate strain rates that correspond to the regime between the quasi-static loading and shock loading.

Acknowledgements

This research was supported by the Office of Naval Research (Dr. Y.D.S. Rajapakse, Scientific Officer) and is gratefully acknowledged. MV gratefully acknowledges the support provided by TÜBİTAK (The Scientific and Technical Research Council of Turkey) through the NATO Advanced Science Fellowship.

References

Ashby, M.F., Evans, A., Fleck, N.A., Gibson, L.J., Hutchinson, J.W., Wadley, H.N.G., 2000. Metal Foams: A Design Guide. Butterworth–Heinemann, London.

Baker, W.E., Togami, T.C., Weydert, J.C., 1998. Static and dynamic properties of high-density metal honeycombs. International Journal of Impact Engineering 21 (3), 149–163.

Calladine, C.R., English, R.W., 1984. Strain-rate and inertia effects in the collapse of two types of energy absorbing structure. International Journal of Mechanical Sciences 26, 689–701.

Cave, I.D., 1968. The anisotropic elasticity of the plant cell wall. Wood Science and Technology 2 (4), 268–278.

Cave, I.D., 1969. The longitudinal Young's modulus of *Pinus radiata*. Wood Science and Technology 3 (1), 40–48.

Chen, W., Lu, F., Zhou, B., 2000. A quartz–crystal-embedded split Hopkinson pressure bar for soft materials. Experimental Mechanics 40 (1), 1–6.

Daigle, D.L., Lonborg, J.O., 1961. Evaluation of certain crushable materials. JPL Technical Report No. 32-120, California Institute of Technology, Pasadena, CA.

Deshpande, V.S., Fleck, N.A., 2000. High strain rate compressive behavior of aluminium alloy foams. International Journal of Impact Engineering 24, 277–298.

Dinwoodie, J.M., 1975. Timber—a review of the structure–mechanical property relationship. Journal of Microscopy 4 (1), 3–32.

Easterling, K.E., Harrysson, R., Gibson, L.J., Ashby, M.F., 1982. On the mechanics of balsa and other woods. Proceedings of the Royal Society of London A 383, 31–41.

Gibson, L.J., Ashby, M.F., 1997. Cellular Solids: Structure and Properties. Cambridge University Press, Cambridge, MA.

Goldsmith, W., Sackman, J.L., 1992. An experimental study of energy absorption in impact on sandwich plates. International Journal of Impact Engineering 12 (2), 241–262.

Harrigan, J.J., Reid, S.R., Peng, C., 1999. Inertia effects in impact energy absorbing materials and structures. International Journal of Impact Engineering 22, 955–979.

Karagiozova, D., Jones, N.A., 1995. A note on the inertia and strain-rate effects in Tam and Calladine model. International Journal of Impact Engineering 16, 637–649.

Knoell, A.C., 1966. Environmental and physical effects of the response of balsa wood as an energy dissipator. JPL Technical Report No. 32-944, California Institute of Technology, Pasadena, CA.

Kolsky, H., 1949. An investigation of mechanical properties of materials at very high rates of loading. Proceedings of the Royal Society of London Series B 62, 676–700.

Maiti, S.K., Gibson, L.J., Ashby, M.F., 1984. Deformation and energy absorption diagrams for cellular solids. Acta Metallurgica 32 (11), 1963–1975.

Mamalis, A.G., Robinson, M., Manolakos, D.E., Demosthenous, G.A., Ioannidis, M.B., Carruthers, J., 1997. Review: Crashworthy capability of composite material structures. Composite Structures 37, 109–134.

Mark, R.E., 1967. Cell Wall Mechanics of Tracheids. Yale University Press, New Haven, CT.

Ravichandran, G., Subhash, G., 1994. Critical appraisal of limiting strain rates for compression testing of ceramics in split Hopkinson pressure bar. Journal of the American Ceramic Society 77 (1), 263–267.

Reid, S.R., Peng, C., 1997. Dynamic uniaxial crushing of wood. International Journal of Impact Engineering 19 (5–6), 531–570.

Soden, P.D., McLeish, R.D., 1976. Variables affecting the strength of balsa wood. Journal of Strain Analysis 11 (4), 225–234.

Su, X.Y., Yu, T.X., Reid, S.R., 1995a. Inertia-sensitive impact energy-absorbing structures. Part I: Effects of inertia and elasticity. International Journal of Impact Engineering 16, 651–672.

Su, X.Y., Yu, T.X., Reid, S.R., 1995b. Inertia-sensitive impact energy-absorbing structures. Part II: Effects of strain-rate. International Journal of Impact Engineering 16, 673–689.

Tam, L.L., Calladine, C.R., 1991. Inertia and strain-rate effects in a simple plate-structure under impact loading. International Journal of Impact Engineering 11, 349–377.

Vural, M., Ravichandran, G., 2003. Microstructural aspects and modeling of failure in naturally occurring porous composites. Mechanics of Materials 35, 523–536.

Wangaard, F.F., 1950. The Mechanical Properties of Wood. John Wiley & Sons, New York.

Wu, E., Jiang, W-S., 1997. Axial crush of metallic honeycombs. International Journal of Impact Engineering 19 (5–6), 439–456.

Zhang, T.G., Yu, T.X., 1989. A note on a velocity sensitive energy absorbing structure. International Journal of Impact Engineering 8, 43–51.

Zhao, H., Gary, G., 1998. Crushing behavior of aluminium honeycombs under impact loading. International Journal of Impact Engineering 21 (10), 827–836.